Fabrication and characterisation of nanocrystalline graphite MEMS resonators using a geometric design to control buckling

Fabrication and characterisation of nanocrystalline graphite MEMS resonators using a geometric design to control buckling

S.J. Fishlock[1-4], S.J. O'Shea[2], J.W. McBride[1,3], H.M.H. Chong[4] and S.H. Pu[1,3,4].

[1]Mechatronics Research Group, Faculty of Engineering and the Environment, University of Southampton, Southampton SO17 1BJ, UK

[2] A*STAR, Institute of Materials Research and Engineering (IMRE) 2 Fusionopolis Way, Innovis, Singapore, 138634

[3]University of Southampton Malaysia Campus, Iskandar Puteri, 79200, Johor, Malaysia

[4]Nanoelectronics and Nanotechnologies Research Group, Electronics and Computer Science, University of Southampton, Southampton SO17 1BJ, UK

The simulation, fabrication and characterisation of nanographite MEMS resonators is reported in this paper. The deposition of nanographite is achieved using plasma-enhanced chemical vapour deposition directly onto numerous substrates such as commercial silicon wafers. As a result, many of the reliability issues of devices based on transferred graphene are avoided. The fabrication of the resonators is presented along with a simple undercutting method to overcome buckling, by changing the effective stress of the structure from ~ 436 MPa compressive, to ~13 MPa tensile. The characterisation of the resonators using electrostatic actuation and laser Doppler vibrometry is reported, demonstrating resonator frequencies from 5 to 640 kHz and quality factor above 1819 in vacuum obtained.

1. Introduction

Carbon-based films such as thin film graphite (multi-layer graphene), graphene and diamond-like carbon (DLC) are emerging materials for use in MEMS/NEMS applications [1–3]. The materials possess good electrical conductivity [4], mechanical properties [5,6] and chemical inertness [7]. Consequently, these carbon thin films have attractive properties for MEMS and NEMS, for example for usage as ultra-sensitive mass and strain sensors [1,8,9] and NEMS switches [10–12].

The commonly used synthesis routes for these materials are not conducive for the scalable fabrication of MEMS/NEMS, however. For example, resonators fabricated using thin films of graphite and single-layer graphene [1], obtained from mechanically exfoliated graphite, are limited in size and shape. Another commonly used synthesis method for graphitic films is using thermal chemical vapour deposition (CVD) onto metal or germanium catalysts [13,14]. However these need to be transferred to a device-compatible substrate, which leads to defects such as wrinkles and tears [15,16], and gives poor control over the strain across the film [17]. The transferal process of graphene from the catalyst to the device substrate is a major issue in reliably fabricating graphenic MEMS and NEMS. DLC films do not require transfer and may be deposited directly onto suitable substrates such as silicon and silicon dioxide, using plasma-enhanced CVD (PECVD) [18] or physical vapour deposition [3].

However, DLC is typically under a high state of stress (~1 to 10 GPa [19]) which commonly leads to buckling [3] of released structures, which has limited the use of DLC in released MEMS.

PECVD nanocrystalline graphite and graphene (nanographite and nanographene) thin films represent a recent material development for carbon-based MEMS and have been used in buckled microstructures [20] and in buckled NEMS switches [12]. Nanographite films are comprised of graphene domains on the order of 30 to 50 nm [20] and may be deposited onto large-scaled substrates such as 150 mm silicon wafers [21]. Nanographite is comprised of sp^2 bonded carbon [22,23] and has a Young's modulus of 23 GPa [20]. The growth of nanographite is non-catalytic and its structure is similar to layers of polycrystalline graphene with nano-scaled grains [12]. Ultra-thin nanographene films of 5 nm thickness have recently been used in NEMS switches with reversible performance and pull-in voltage < 3V [12]. Nanographite has been used in various electrical applications such as Schottky diodes [24], Schottky diode photodetectors [25], photovoltaics [26], transparent conducting electrodes [21] and strain gauges [27].

Suspended nanographite structures, like DLC and graphene NEMS structures, often suffer from buckling [3,12,20,28]. The buckling is due to large built-in compressive stresses of the thin films, and is generally deleterious to the performance of released MEMS and NEMS, since the large non-linear deflection of the structure is difficult to model and creates difficulty in device performance. Previous work on released nanographite structures and switches showed the promise of nanographite-based MEMS and NEMS, although there was no clear method to fabricate freestanding structures with no buckling.

This work demonstrates the fabrication and characterisation of nanographite MEMS resonators. A method to fabricate the structures without buckling using standard micromachining is reported. This work further highlights nanographite as a promising material for MEMS, by measuring the resonator properties of suspended cantilever and beam structures.

2. Deposition and device design

2.1 Deposition and material characterisation

Nanographite films were deposited onto 150 mm diameter silicon wafers using a commercial PECVD tool (Oxford Instruments Nanofab1000 Agile). The deposition conditions are summarised in table 1. The carbon precursor is CH_4, which is dissociated into various free radicals such as CH_x, C_2H_y, C_3H_z during the reaction [23]. The H_2 acts as a diluent, controlling deposition rate and promoting graphitic

carbon growth by etching amorphous carbon [29]. A deposition rate of approximately 2 nm per minute was measured with the conditions described in table1.

Temperature (°C)	750
RF power (W)	100
Chamber pressure (mTorr)	1500
CH_4 flow (sccm)	75
H_2 flow (sccm)	60

Table 1. Summary of PECVD deposition conditions for nanographite.

Raman spectroscopy (Renishaw inVia) was used to characterise the structural properties of the nanographite film, using a 532 nm wavelength excitation laser. A Raman spectrum obtained from a nanographite thin film is shown in figure 1, with the main peaks highlighted. The D peak at 1350 cm^{-1} arises from defects within the graphite lattice, such as grain boundaries and dislocations [30]. The G (1593cm^{-1}) and 2D (2690 cm^{-1}) peaks arise from graphitic bonded carbon. D+D' (2934 cm^{-1}) is related to the defects in the material. The amplitude of the D peak with respect to the G peak I_D/I_G of 1.7 shows that this is nanocrystalline graphite [31]. X-ray reflectivity was performed on a nanographite film (Panalytical X'pert Pro X-ray diffractometer). The fitted data was used to obtain the mass density of 1900 kg m^{-3}.

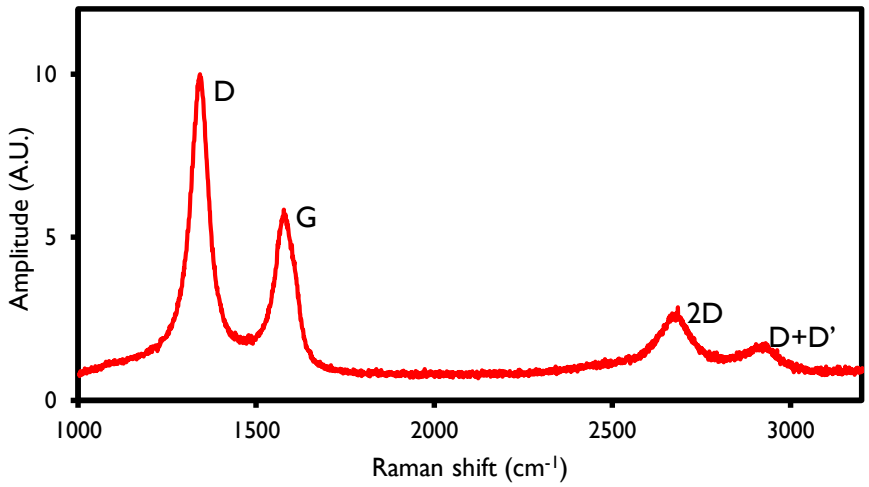

Figure 1. Raman spectrum of a nanographite film taken with 532 nm excitation laser.

2.2 Microfabrication process flow

The fabrication process for the nanographite cantilevers and doubly-clamped beam resonators is summarised here. Firstly, 200 nm SiO_2 is deposited using PECVD, and then 270 to 350 nm nanographite is deposited directly onto the SiO_2, figure 2(a). The device outline, a rectangular beam with large (200 μm^2) square anchors, is then patterned using UV lithography and both SiO_2 and

nanographite layers were fully etched using CHF_3- and O_2-based RIE, respectively. Titanium/nickel electrodes of 5/50 nm thickness are deposited over the wafer using e-beam evaporation (Leybold LAB700) and patterned using lift-off, figure 2(b). The final step is to release the 10 μm-wide beam structures from the substrate using HF vapour, figure 2(c).

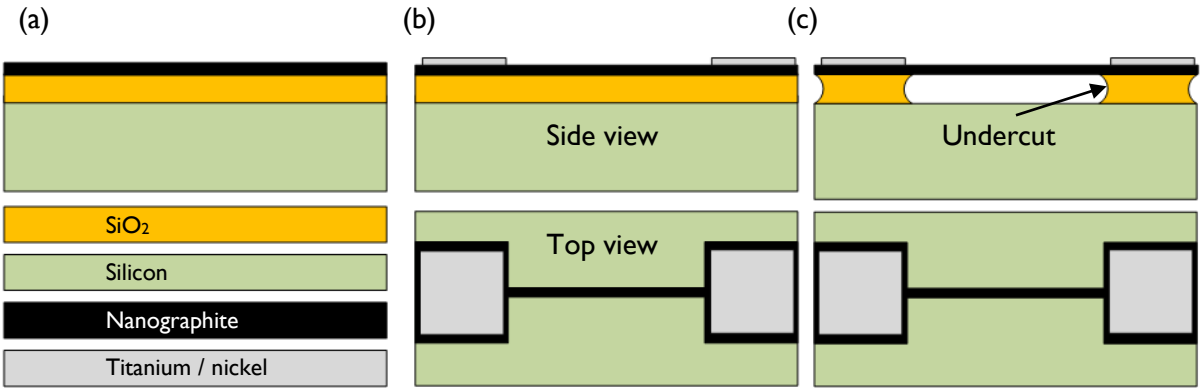

Figure 2. Schematic of the main steps in fabrication of the nanographite resonators. a) The starting material stack. b) The patterned structure, in this example a doubly-clamped beam. c) The released structure.

A relatively large undercut of the beam anchors, caused by over-etching during the isotropic HF vapour release stage, enables buckle-free structures to be fabricated because the deformation of the beam anchors can be adjusted during the etch process such that the beam moves from a buckled state to a flat, tensile state. This process is illustrated in figure 3, showing the evolution in profile for a released beam. Figure 3(a) shows the beam in the initial buckled state, while figure 3(b) shows the straightened beam after being effectively pulled into a state of tensile stress as the undercut length increases during etching. The final undercut length is 25 μm, measured using optical microscope. The initial stress was calculated using the wafer bow method [32] as 436 ± 20 MPa compressive. These devices were etched using HF vapour, with 25 % HF diluted in deionised water. A completed doubly-clamped beam device is shown in figure 3(c).

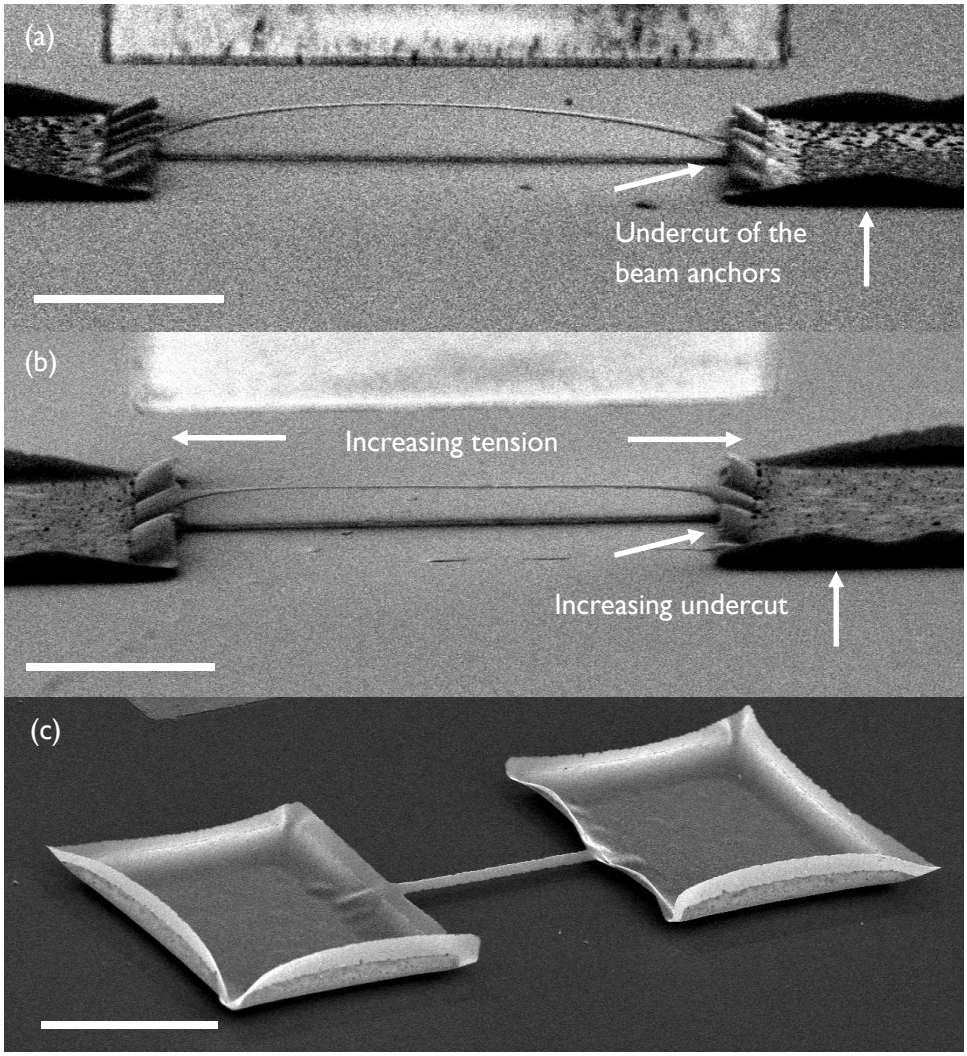

Figure 3. (a-b) Scanning electron micrographs of the increasing undercut process leading to tensile stress of a doubly-clamped beam. (c) A completed 100 μm long doubly-clamped nanographite beam. Scales bars: (a-b) 50 μm, (c) 100 μm.

2.3 Design of cantilever resonators

The resonator structures may be modelled as beams, either clamped-free (cantilever) or doubly-clamped beams (see Section 2.4). The fundamental or natural resonant frequency f_0 of cantilever beam with rectangular cross section is [33],

$$f_0 = 0.162\sqrt{\frac{E}{\rho}}\left(\frac{h}{L^2}\right) \quad (1)$$

where E is the Young's modulus, ρ is density and thickness is h and L is the length. However, the fabricated resonator structures have two main imperfections which cause deviation from the ideal values of f_0: (i) there is an undercut of the beam, which adds an effective length ΔL [34,35] to the beam, since this section is free to deflect and is therefore compliant; (ii) there is curvature of the cantilever beam and anchors caused by a stress gradient σ_{grad} through the thickness of the film. σ_{grad} is assumed to be linear and can be calculated [36],

$$\sigma_{grad} = \frac{\kappa h}{2}\frac{E}{(1-\nu)} \quad (2)$$

where κ is the curvature and ν is the Poisson ratio. The curvature of released cantilever beams can be measured by SEM inspection, and in this work the stress gradient for a typical graphite cantilever (5 cantilevers of length 75 to 150μm, width 10 μm, thickness 350 nm were measured) σ_{grad} was calculated as 49.5 MPa, taking E and ν as 23 GPa and 0.25 respectively [20].

To take account of the two fabrication imperfections of the structure, the cantilever beams of length 75, 100 and 150 μm long, 10 μm width and 350 nm thick were modelled using finite element (FE) analysis. A 25 μm undercut was included for all beams. The FE model used 2D, layered, shell elements, and σ_{grad} was modelled by applying a linear variation in the thermal expansion coefficient of each layer of the shell such that the defined thermal stress gradient was equal to the experimentally measured σ_{grad}= 49.5 MPa and the average stress σ_0 was 436 MPa compressive.

Firstly, note that changes in cantilever resonance frequency due to small changes in curvature (i.e. bending) are negligible [37]. Thus the stress has negligible effect on the resonance frequencies of the released cantilevers [38], essentially because the cantilever has a free end to allow deformation or bending which relieves the stress, although the presence of a total (i.e. nett) surface stress can be important for ultrathin cantilevers [39]. Given that the simulation results of resonant frequency (see figure 4) yield a consistently lower value of f_0 than the result of equation (1) using the cantilever length (L), we conclude this discrepancy is primarily due to the extra length ΔL caused by the undercut. By simply modifying equation (1) to include ΔL, as shown by equation (3) below, in principle the analytical expression can be made to match the FE calculations by a suitable choice of ΔL, as shown in figure 4.

In this example ΔL was found to be 4.85 μm. However, the actual undercut L_u is 25 μm. Gavan *et al* [30] observed a similar result on the effect of undercut using silicon nitride cantilevers, finding a ΔL value of 6.7 μm whereas the undercut L_u=12.5 μm. This effect arises because the relatively greater width of the overhang means the overhang section is less compliant than the beam due to the higher value of the second moment of area, and thus $L_u > \Delta L$.

$$f_0 = 0.162\sqrt{\frac{E}{\rho}}\left(\frac{h}{(L+\Delta L)^2}\right) \tag{3}$$

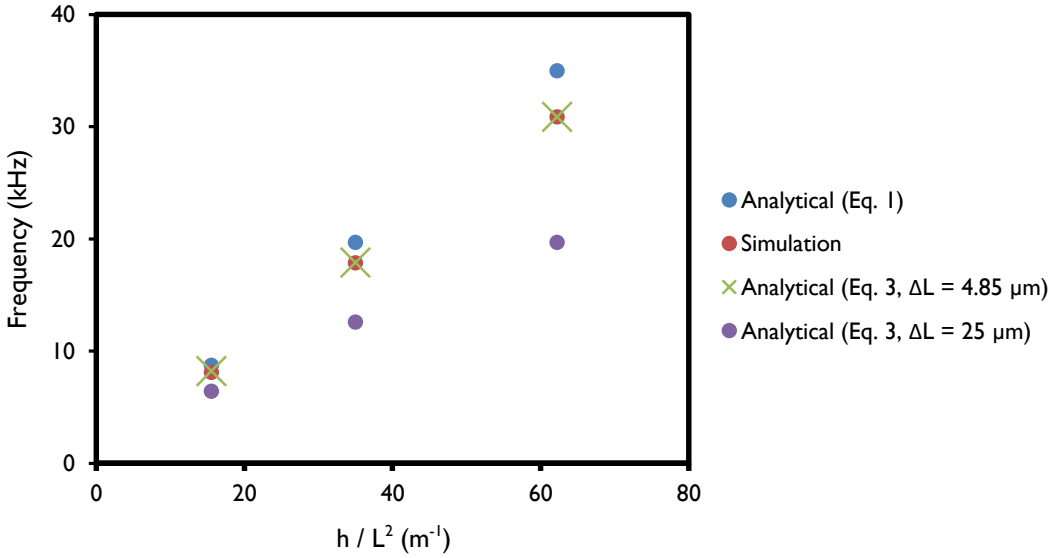

Figure 4. Comparison of the natural frequency of cantilevers, calculated using FE simulation (L = 75, 100, 150μm, w=10 μm, h = 350 nm, σ_{grad} = 49.5 MPa, undercut L_u= 25 μm) and two analytical methods (equation (1) and equation (3) with ΔL = 4.85 μm and ΔL = 25 μm).

Plotting equation (3) using the actual undercut value of L_u=25 μm, see figure 4, gives resonance frequencies which are far too low compared with the simulation result. Thus, simple analytical expressions such as equation (3) can only provide an approximate value of a cantilever resonance. This is not surprising given that the width of a cantilever varies in the undercut section and this changes the resonance [35], yet equation (3) does not explicitly contain terms in the width. More accurate calculations of resonance frequency can be made using either analytical or finite element methods [40,41] but given the many experimental uncertainties in the fabrication of thin nanographite films (e.g. variations in E, ρ, and thickness), equation (3) is probably adequate for most design purposes.

2.4 Design of doubly-clamped beam resonators

Doubly clamped beams were modeled with the same material and stress parameters (σ_0 = 436 MPa and σ_{grad}= 49.5 MPa) as for the cantilevers, and using beam lengths of 75, 100 and 150 μm. Finite Element modeling is the preferred model approach as analytical expressions for clamped beams with compressive stress are overly complicated for our purposes, and in particular for buckled beams. Static FE analysis shows the mechanism by which the doubly-clamped beams progress from a buckled and compressive state to a tensile-stress state, as highlighted in figure 5 (a-e). At zero and small undercuts, the doubly-clamped beam may be considered as a beam with rigid anchors. The built-in stress of the beam is compressive, and the magnitude (436 MPa) is higher than the critical buckling stress, which is approximately ~1 MPa as given by the Euler buckling limit $\sigma_{Euler} = -\frac{\pi^2}{3}\frac{Eh^2}{L^2}$ [31]. Thus, the beam buckles upwards as shown in figure 5 (a-b). At zero undercut, the doubly-clamped beam is buckled upward with a maximum amplitude of 13.4 μm. Note that the buckled amplitude of the beams observed in SEM, as in figure 3, is also of the order 10 to 15 μm. With a slight undercut of 10 μm, figure 5(b), the beam is still buckled with an increased amplitude of 15.5 μm. The higher amplitude is caused by the additional deflection as the anchors start to deflect and deform away from the substrate, as the biaxial stress causes a periodic rippling in the released overhang section. The wavelength of the overhang rippling increases as the undercut becomes larger (15 μm), as visible in figure 5 (c), where the beam starts to 'flatten' out, transitioning from a typical sinusoidal buckled shape to a flatter curve, with a maximum amplitude of 14.2 μm. At a 25 μm undercut, as shown in figure 5 (d) the wavelength of the overhang ripple is large compared to the anchor width. The stress becomes tensile at both ends of the beam, which effectively 'pulls' the beam tight, yielding a beam which is under tensile stress and does not suffer from buckling. The stress intensity is shown in figure 5 (e), and shows that the beam section is under a 12.9 MPa tensile stress σ_t at undercut L_u= 25 μm.

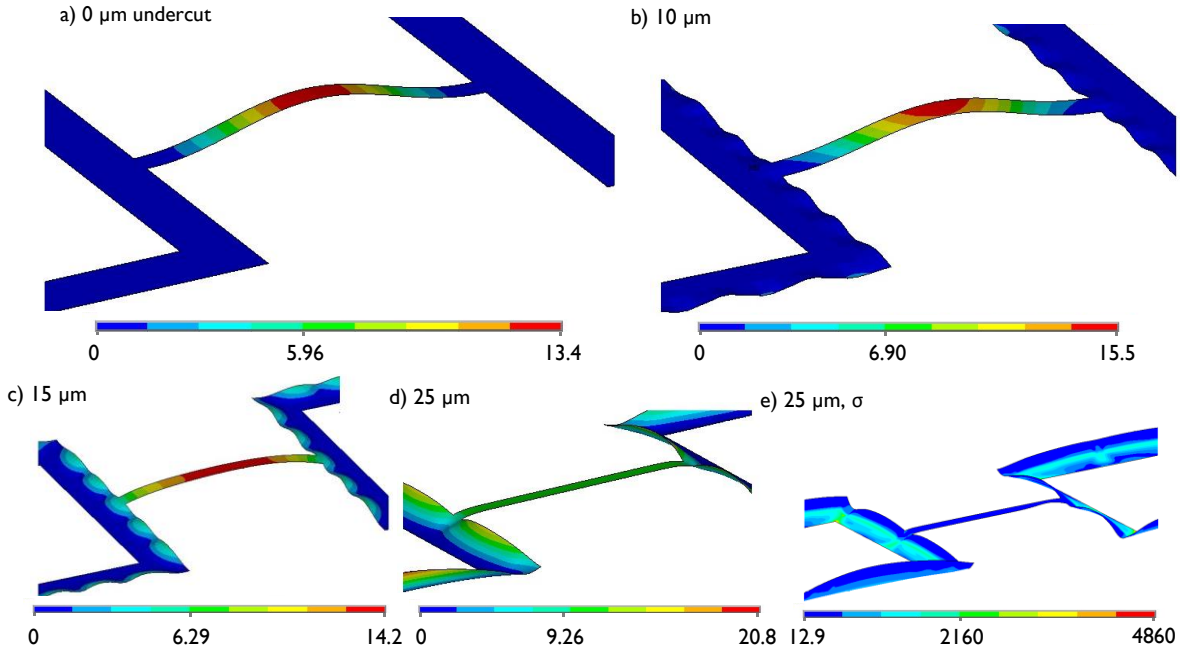

Figure 5. Simulation showing the transition of doubly-clamped beams from buckling to tensile stress with an increasing undercut. (a-d) colour contouration show the deflection in µm for different undercut values, and (e) colour contouration shows the stress intensity in MPa for the 25 µm undercut beam.

The fundamental resonance frequency of a doubly-clamped beam with an undercut, which is not buckled and is under tensile stress (σ_t), may be modelled analytically by [35],

$$f_0 = \left(1.03\frac{h}{(L+2\Delta L)^2}\sqrt{\frac{E}{\rho}}\right)\sqrt{1+\frac{\sigma_t(L+2\Delta L)^2}{3.4Eh^2}} \qquad (4)$$

where, as described previously, the extra length ΔL is incorporated into the standard expression to account for the undercut. As the geometric undercut is equal to that of the cantilevers (each are etched in the same procedure), the value of ΔL is assumed to be identical for the doubly clamped beams.

2.5 Experimental characterisation of resonators

The released devices were electrostatically actuated by applying a voltage $V = V_{DC} + V_{AC} \cdot cos\ (2\pi ft)$ between the beam and the grounded silicon substrate. Here V_{DC} is the DC bias and V_{AC} is the amplitude of the AC voltage bias, applied at frequency f. This generates an electrostatic force F_e applied to the beam which, ignoring high order terms in V_{ac}, may be calculated as [42],

$$F_e \approx -\frac{1}{2}\frac{\partial C}{\partial r}\left(V_{DC}^2 + 2V_{DC}V_{ac}\cos\left(2\pi ft\right)\right) \qquad (5)$$

where C is the effective capacitance between the resonator area and the underlying substrate at a separation distance r. As the forcing frequency f becomes close to the natural frequency of vibration of the mechanical beam, the vibration amplitude becomes large. During testing of the nanographite devices, a DC bias of 2 V and AC voltage of 0.2 V was applied using a voltage function generator (HP 33120A). A commercial LDV system (Polytec 300-F) was used to measure the vibrational velocity of the beam during actuation and find the resonance frequencies of the devices. An automated sweep of the frequency f of the AC voltage signal V_{AC} was performed between 0 and 1 MHz. If required, testing can be undertaken in vacuum conditions to decrease viscous air damping and hence facilitate actuation and detection of the beam oscillations. A custom-built vacuum chamber was used with the base pressure less than 30 mTorr as measured by a manometer gauge (MKS Baratron). An O-ring sealed window allowed the LDV laser to pass and focus on the device.

3. Results and discussion

The resonators were characterised by measuring their natural frequency and Q. The majority of the results were performed in ambient conditions. Only one device, a doubly clamped beam, was wire bonded to enable testing under vacuum.

For cantilever beams, eleven resonator structures from four separate chips were used. The thickness of the nanographite on each chip was measured by stylus profilometry with values between 270 and 340 nm. Cantilevers of L between 75 to 150 μm were measured, with frequencies in the range of 5.3 to 27.0 kHz and Q of 5 to 10 in air. Figure 6 shows the f_0 data plotted against $h\ /(L+\Delta L)^2$, with the dashed line indicating values as calculated by equation (3) using E = 23 GPa [20] and ΔL = 4.85 μm. Given the simplicity of equation (3), the analytical and experimental values are in reasonable agreement. The actual undercut was measured by optical microscope as L_u=25 μm and was approximately the same for all cantilevers.

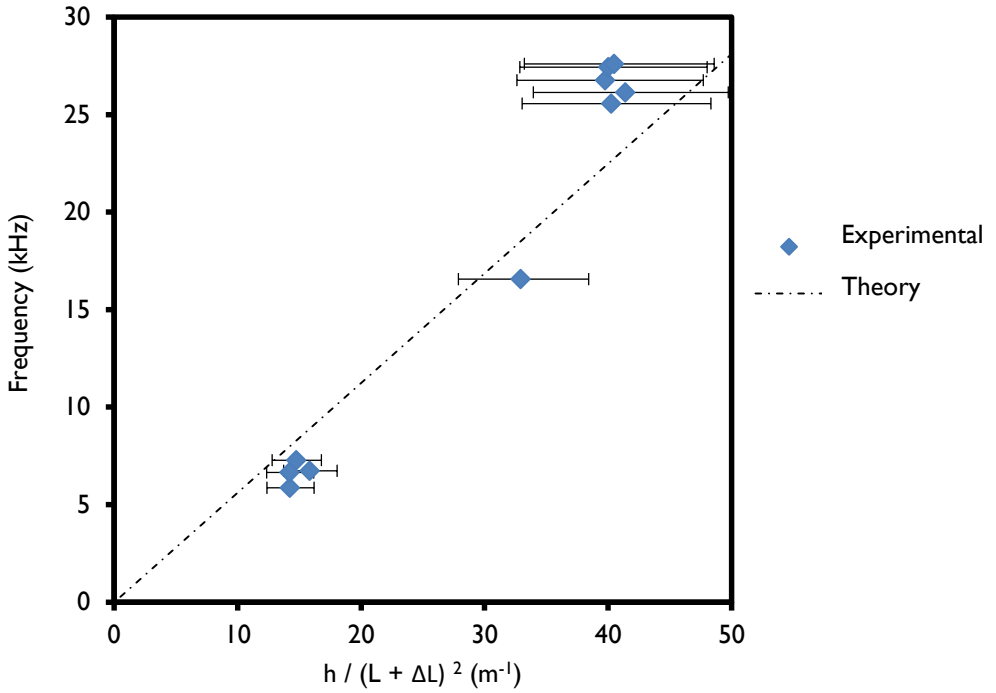

Figure 6. Natural frequency of cantilever beams of length 75 to 150 μm. The dotted line is the theoretical result, Equation (3), of the fundamental frequency of cantilever beams using E = 23 GPa and ΔL= 4.85 μm. The error bars indicated primarily arise from uncertainty in the thickness of the beams.

The resonance properties of fourteen doubly-clamped beams were characterised in the same way as the cantilevers, with one device also being tested under vacuum. The doubly clamped beams had L of 75, 100 and 150 μm and h of 270 to 340 nm. The undercut of all devices were measured as approximately 25 μm for all the devices. Figure 7 shows the fundamental frequency of the doubly-clamped beams, plotted against $h/(L+\Delta L)^2$, where ΔL is 4.85 μm. The structures have natural frequencies of 566 to 640 kHz (L =75 μm), 376 to 474 kHz (L =100 μm) and 245 to 267 kHz (L =150 μm). The results are compared with equation (4), using the value of σ_t= 12.9 MPa obtained using the FE simulation. Reasonable agreement is observed, indicating that equation (4) can provide approximate results for designing doubly-clamped resonator structures.

The inset of figure 7 shows the frequency response of a doubly-clamped beam of length 100 μm under vacuum. The Q value of the resonance peak is >1819, which is considerably higher than any value measured under ambient conditions, where Q is typically under 10.

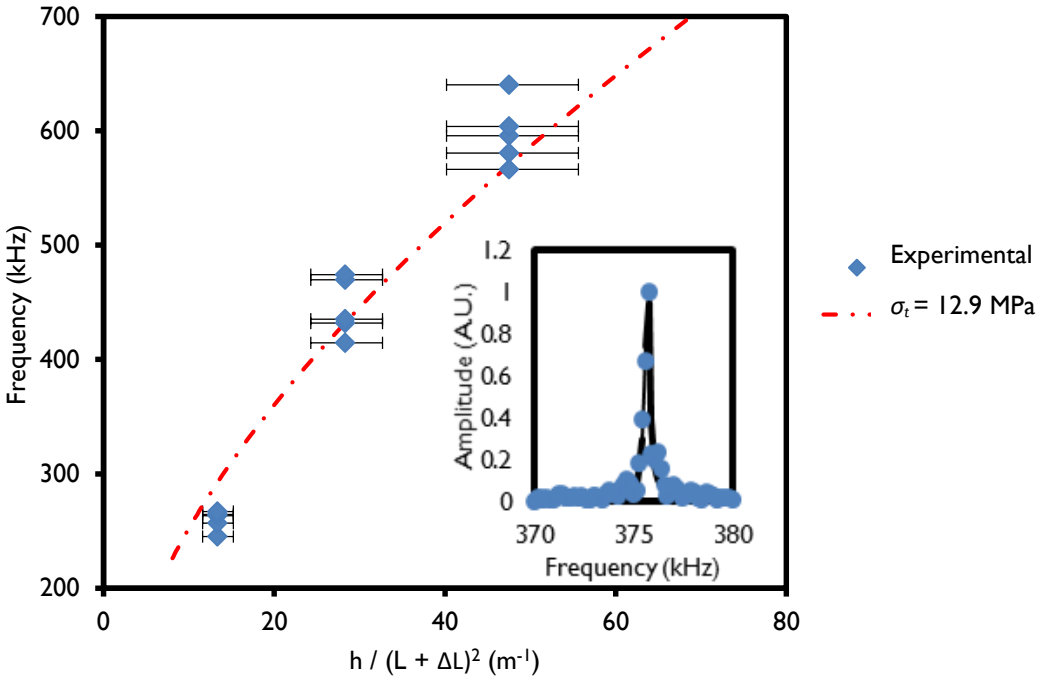

Figure 7. Natural frequency of doubly-clamped beams of length 75 to 150 μm, measured at ambient pressure. The dashed lines show the theoretical resonance frequency, equation (4), using ΔL= 4.85 μm and stress σ_τ =12.9 MPa. The error bars indicated primarily arise from uncertainty the thickness of the beams. Inset shows the frequency response of a 100 μm doubly-clamped beam under vacuum with the fitted Lorentzian (black line) giving Q~ 1819.

The devices fabricated are from a material with high compressive stress (436 MPa), but the results of this work nevertheless demonstrate that under cutting the anchors can produce unbuckled beams under an effective tensile stress σ_t of 12.9 MPa. The curvature and geometry of the anchors caused by σ_{grad} creates a resultant deflection of the anchors, which in turn imparts a tensile stress to the beam section of the device.

Undercutting the anchors is a simple way to obtain tensile-stressed structures from a compressively-stressed material. This could have potential applications for different types of MEMS devices. For example, many doubly-clamped beam structures fabricated from carbon thin films such as DLC, nanographite and graphene appear to suffer from buckling [3,12,43], which greatly increases unreliability and irreproducibility. Furthermore, the stiffness and geometry of an out-of-plane MEMS or NEMS switching device could be trimmed using this undercut method, thereby altering the pull-in voltage.

4. Conclusions

The fabrication and characterisation of MEMS nanographite resonators has been presented. The deposition of nanographite was achieved using PECVD, and this enabled fabrication of devices using standard MEMS micromachining technology.

Although the material is under a high compressive stress, undercutting the anchors of the beam structures enables the stress gradient σ_{grad} in the film to lift up the beam anchors, and thereby 'pull' the beam tight. This is a technique which may be of wide-ranging interest, as a large number of carbon doubly-clamped devices suffer from buckling [3,12,43]. The large-scale and reproducible synthesis route of nanographite is well-suited for MEMS and NEMS applications, and the results show that nanographite is a promising material for MEMS resonators. Furthermore, due to the electrical conductivity, low Young's modulus of 23 GPa [20], and low stiction compared with metals [11], nanographite is a very attractive material for NEMS switches [12].

5. Acknowledgements

The author's gratefully acknowledge funding from the Faculty of Engineering and the Environment, University of Southampton, IMRE, A*STAR under the ARAP programme, and Malaysian Ministry of Higher Education grant FRGS/2/2014/TK03/USMC/02/1.

References

[1] J.S. Bunch, A.M. van der Zande, S.S. Verbridge, I.W. Frank, D.M. Tanenbaum, J.M. Parpia, H.G. Craighead, P.L. McEuen, Electromechanical resonators from graphene sheets., Science. 315 (2007) 490–3. doi:10.1126/science.1136836.

[2] A.M. Van Der Zande, R. a Barton, J.S. Alden, C.S. Ruiz-Vargas, W.S. Whitney, P.H.Q. Pham, J. Park, J.M. Parpia, H.G. Craighead, P.L. McEuen, Large-Scale Arrays of Single-Layer Graphene Resonators., Nano Letters. (2010) 4869–4873. doi:10.1021/nl102713c.

[3] M. Tomi, A. Isacsson, M. Oksanen, D. Lyashenko, J.P. Kaikkonen, S. Tervakangas, J. Kolehmainen, P.J. Hakonen, Buckled diamond-like carbon nanomechanical resonators, Nanoscale. 7 (2015) 14747–14751. doi:10.1039/C5NR02820E.

[4] K.I. Bolotin, K.J. Sikes, Z. Jiang, M. Klima, G. Fudenberg, J. Hone, P. Kim, H.L. Stormer, Ultrahigh electron mobility in suspended graphene, Solid State Communications. 146 (2008) 351–355. doi:10.1016/j.ssc.2008.02.024.

[5] G.-H. Lee, R.C. Cooper, S.J. An, S. Lee, A. van der Zande, N. Petrone, A.G. Hammerberg, C. Lee, B. Crawford, W. Oliver, J.W. Kysar, J. Hone, High-strength chemical-vapor-deposited graphene and grain boundaries., Science (New York, N.Y.). 340 (2013) 1073–6. doi:10.1126/science.1235126.

[6] E. Peiner, A. Tibrewala, R. Bandorf, H. Lüthje, L. Doering, W. Limmer, Diamond-like carbon for MEMS, Journal of Micromechanics and Microengineering. 17 (2007) S83–S90. doi:10.1088/0960-1317/17/7/S04.

[7] M. Wissler, Graphite and carbon powders for electrochemical applications, Journal of Power Sources. 156 (2006) 142–150. doi:10.1016/j.jpowsour.2006.02.064.

[8] C. Chen, S. Rosenblatt, K.I. Bolotin, W. Kalb, P. Kim, I. Kymissis, H.L. Stormer, T.F. Heinz, J. Hone, Performance of monolayer graphene nanomechanical resonators with electrical readout., Nature Nanotechnology. 4 (2009) 861–7. doi:10.1038/nnano.2009.267.

[9] H. Lee, W. Chang, H. Lee, Y. Yang, W.C. Ã, Mass Detection Using a Graphene-Based Nanomechanical Resonator, Japanese Journal of Applied Physics. 52 (2013).

[10] J. Sun, W. Wang, M. Muruganathan, H. Mizuta, Low pull-in voltage graphene electromechanical switch fabricated with a polymer sacrificial spacer, Applied Physics Letters. 105 (2014) 33103. doi:10.1063/1.4891055.

[11] O. Loh, X. Wei, J. Sullivan, L.E. Ocola, R. Divan, H.D. Espinosa, Carbon-Carbon Contacts for Robust Nanoelectromechanical Switches, Advanced Materials. 24 (2012) 2463–2468. doi:10.1002/adma.201104889.

[12] J. Sun, M.E. Schmidt, M. Muruganathan, H.M.H. Chong, H. Mizuta, Large-scale nanoelectromechanical switches based on directly deposited nanocrystalline graphene on insulating substrates, Nanoscale. 8 (2016) 6659–6665. doi:10.1039/C6NR00253F.

[13] X. Li, W. Cai, J. An, S. Kim, J. Nah, D. Yang, R. Piner, A. Velamakanni, I. Jung, E. Tutuc, S.K. Banerjee, L. Colombo, R.S. Ruoff, Large-area synthesis of high-quality and uniform graphene films on copper foils., Science. 324 (2009) 1312–4. doi:10.1126/science.1171245.

[14] J. Lee, E.K. Lee, W. Joo, Y. Jang, B. Kim, J.Y. Lim, S. Choi, S.J. Ahn, J.R. Ahn, M. Park, C. Yang, B.L. Choi, S. Hwang, D. Whang, Wafer-Scale Growth of Single-Crystal Monolayer Graphene on Reusable Hydrogen-Terminated Germanium, Science. 344 (2014) 286–289. doi:10.1126/science.1252268.

[15] C.S. Ruiz-Vargas, H.L. Zhuang, P.Y. Huang, A.M. van der Zande, S. Garg, P.L. McEuen, D. a Muller, R.G. Hennig, J. Park, Softened elastic response and unzipping in chemical vapor deposition graphene membranes., Nano Letters. 11 (2011) 2259–63. doi:10.1021/nl200429f.

[16] K.M. Milaninia, M.A. Baldo, A. Reina, J. Kong, All graphene electromechanical switch fabricated by chemical vapor deposition, Applied Physics Letters. 95 (2009) 183105. doi:10.1063/1.3259415.

[17] A.M. Van Der Zande, R.A. Barton, J.S. Alden, C.S. Ruiz-Vargas, W.S. Whitney, P.H.Q. Pham, J. Park, J.M. Parpia, H.G. Craighead, P.L. McEuen, Large-scale arrays of single-layer graphene resonators, Nano Letters. 10 (2010) 4869–4873. doi:10.1021/nl102713c.

[18] N. Ravi, V.L. Bukhovets, I.G. Varshavskaya, G. Sundararajan, Deposition of diamond-like carbon films on aluminium substrates by RF-PECVD technique: Influence of process parameters, Diamond and Related Materials. 16 (2007) 90–97. doi:10.1016/j.diamond.2006.04.001.

[19] J.K. Luo, Y.Q. Fu, H.R. Le, J.A. Williams, S.M. Spearing, W.I. Milne, Diamond and diamond-like carbon MEMS, Journal of Micromechanics and Microengineering. 17 (2007) S147–S163. doi:10.1088/0960-1317/17/7/S12.

[20] S.J. Fishlock, D. Grech, J.W. McBride, H.M.H. Chong, S.H. Pu, Mechanical characterisation of nanocrystalline graphite using micromechanical structures, Microelectronic Engineering. 159 (2016) 184–189. doi:10.1016/j.mee.2016.03.040.

[21] M.E. Schmidt, C. Xu, M. Cooke, H. Mizuta, H.M.H. Chong, Metal-free plasma-enhanced chemical vapor deposition of large area nanocrystalline graphene, Materials Research Express. 1 (2014) 25031. doi:10.1088/2053-1591/1/2/025031.

[22] H. Medina, Y.C. Lin, C.H. Jin, C.C. Lu, C.H. Yeh, K.P. Huang, K. Suenaga, J. Robertson, P.W. Chiu, Metal-Free Growth of Nanographene on Silicon Oxides for Transparent Conducting Applications, Advanced Functional Materials. 22 (2012) 2123–2128. doi:10.1002/adfm.201102423.

[23] L. Zhang, Z. Shi, Y. Wang, R. Yang, D. Shi, G. Zhang, Catalyst-free growth of nanographene films on various substrates, Nano Research. 4 (2010) 315–321. doi:10.1007/s12274-010-0086-5.

[24] S.M. Sultan, S.H. Pu, S.J. Fishlock, L.H. Wah, S. Member, H.M.H. Chong, J.W. Mcbride, S.

Member, Electrical behavior of Nanocrystalline graphite / p-Si Schottky Diode, in: Proceedings of the 16th International Conference on Nanotechnology, Sendai, Japan, 2016: pp. 307–310.

[25] Z. Zhang, Y. Guo, X. Wang, D. Li, F. Wang, S. Xie, Direct Growth of Nanocrystalline Graphene/Graphite Transparent Electrodes on Si/SiO 2 for Metal-Free Schottky Junction Photodetectors, Advanced Functional Materials. 24 (2014) 835–840. doi:10.1002/adfm.201301924.

[26] G. Kalita, M.S. Kayastha, H. Uchida, K. Wakita, M. Umeno, Direct growth of nanographene films by surface wave plasma chemical vapor deposition and their application in photovoltaic devices, RSC Advances. 2 (2012) 3225–3230. doi:10.1039/c2ra01024k.

[27] J. Zhao, G. Wang, R. Yang, X. Lu, M. Cheng, C. He, G. Xie, J. Meng, D. Shi, G. Zhang, Tunable piezoresistivity of nanographene films for strain sensing., ACS Nano. 9 (2015) 1622–9. doi:10.1021/nn506341u.

[28] N. Lindvall, J. Sun, G. Abdul, A. Yurgens, Towards transfer-free fabrication of graphene NEMS grown by chemical vapour deposition, Micro & Nano Letters. 7 (2012) 749. doi:10.1049/mnl.2012.0211.

[29] W. Yang, C. He, L. Zhang, Y. Wang, Z. Shi, M. Cheng, G. Xie, D. Wang, R. Yang, D. Shi, G. Zhang, Growth, characterization, and properties of nanographene., Small. 8 (2012) 1429–35. doi:10.1002/smll.201101827.

[30] M.A. Pimenta, G. Dresselhaus, M.S. Dresselhaus, L.G. Cançado, A. Jorio, R. Saito, Studying disorder in graphite-based systems by Raman spectroscopy, Physical Chemistry Chemical Physics. 9 (2007) 1276. doi:10.1039/b613962k.

[31] A.C. Ferrari, J. Robertson, Interpretation of Raman spectra of disordered and amorphous carbon, Physical Review B. 61 (2000) 14095–14107. doi:10.1103/PhysRevB.61.14095.

[32] B.K. Tay, D. Sheeja, L.. Yu, On stress reduction of tetrahedral amorphous carbon films for moving mechanical assemblies, Diamond and Related Materials. 12 (2003) 185–194. doi:10.1016/S0925-9635(03)00021-9.

[33] S. Timoshenko, Vibration problems in engineering, D. Van Nostrand Company, INC., New York, USA, 1937. doi:10.1016/S0016-0032(29)91051-6.

[34] L. Kiesewetter, J.M. Zhang, D. Houdeau, A. Steckenborn, Determination of Young Moduli of Micromechanical Thin-Films Using the Resonance Method, Sensors and Actuators A-Physical. 35 (1992) 153–159. doi:10.1016/0924-4247(92)80154-U.

[35] K.B. Gavan, E. van der Drift, W.J. Venstra, M.R. Zuiddam, H.S.J. van der Zant, Effect of undercut on the resonant behaviour of silicon nitride cantilevers, Journal of Micromechanics and Microengineering. 19 (2009) 8. doi:035003\r10.1088/0960-1317/19/3/035003.

[36] S.D. Senturia, Microsystem Design, Kluwer Academic Publishers, Dortrecht, Netherlands, 2001. doi:10.1017/CBO9781107415324.004.

[37] F. Shen, P. Lu, S.J. O'Shea, K.H. Lee, T.Y. Ng, Thermal effects on coated resonant microcantilevers, Sensors and Actuators, A: Physical. 95 (2001) 17–23. doi:10.1016/S0924-4247(01)00715-4.

[38] M.E. Gurtin, X. Markenscoff, R.N. Thurston, Effect of surface stress on the natural frequency of thin crystals, Applied Physics Letters. 29 (1976) 529–530. doi:10.1063/1.89173.

[39] M.J. Lachut, J.E. Sader, Effect of Surface Stress on the Stiffness of Cantilever Plates, Physical Review Letters. 99 (2007) 206102. doi:10.1103/PhysRevLett.99.206102.

[40] S.K. Jang, C.W. Bert, Free vibration of stepped beams: Exact and numerical solutions, Journal of Sound and Vibration. 130 (1989) 342–346. doi:10.1016/0022-460X(89)90561-0.

[41] J.W. Jaworski, E.H. Dowell, Free vibration of a cantilevered beam with multiple steps: Comparison of several theoretical methods with experiment, Journal of Sound and Vibration. 312 (2008) 713–725. doi:10.1016/j.jsv.2007.11.010.

[42] V. Lindroos, M. Tilli, A. Lehto, T. Motooka, T. Veijola, Handbook of Silicon Based MEMS Materials and Technologies, Elsevier Inc., Oxford, UK, 2010. doi:10.1016/B978-0-8155-1594-4.00014-0.

[43] S. Shivaraman, R.A. Barton, X. Yu, J. Alden, L. Herman, M.V.S. Chandrashekhar, J. Park, P.L. Mceuen, J.M. Parpia, H.G. Craighead, M.G. Spencer, Free-Standing Epitaxial Graphene, Nano Letters. 9 (2009) 1–6. doi:10.1021/nl900479g.